Journal of Physics and Chemistry of Solids 160 (2022) 110304

Contents lists available at ScienceDirect

Journal of Physics and Chemistry of Solids

journal homepage: www.elsevier.com/locate/jpcs

The NV^0 defects in diamond: A quantum mechanical characterization through its vibrational and Electron Paramagnetic Resonance spectroscopies

Anna Maria Ferrari [a,*], Maddalena D'Amore [a,**], Khaled E. El-Kelany [b,c], Francesco Silvio Gentile [d], Roberto Dovesi [a]

[a] Dipartimento di Chimica, Università di Torino and NIS (Nanostructured Interfaces and Surfaces) Centre, Via P. Giuria 5, 10125 Torino, Italy
[b] Institute of Nanoscience and Nanotechnology, Kafrelshiekh University, 33516, Kafrelskeikh, Egypt
[c] Dipartimento di Chimica, Università di Torino, Via P. Giuria 5, 10125 Torino, Italy
[d] Department of Chemical Sciences, University of Napoli Federico II, Complesso Universitario di Monte Sant'Angelo – Via Cintia, 21 – 80126 – Napoli, Italy

ARTICLE INFO

Keywords:
NV^0defect
Diamond
Electron paramagnetic resonance (EPR)
IR spectrum
Raman spectrum
B3LYP functional
Gaussian basis
CRYSTAL code
First principles calculations

ABSTRACT

The NV^0 defect in diamond has been investigated quantum-mechanically, by analyzing its structural, electronic, vibrational and magnetic properties. The possible spin states for NV^0 are a quartet NV^0_q ($^4A_2$ symmetry) and a doublet (^2E symmetry). In the latter state a single electron occupies a double degenerate level producing a Jahn Teller distortion that removes the degeneracy and lowers the total energy. The symmetry reduces from C_{3v} to C_S and two local minima are indeed identified, to be indicated as NV^0_{d1} ($^2A'$ symmetry) and NV^0_{d2} ($^2A''$ symmetry). NV^0_{d1} is the ground state, and is more stable than NV^0_q by ~ 0.5 eV, and than NV^0_{d2} by ~ 0.2 eV, irrespective of the functional or basis set adopted.

The EPR hyperfine coupling tensor has been computed for NV^0_q and has been found to be in excellent agreement with available experimental data. The IR spectra of the NV defects (the three neutral cases and also the negatively charged one, for comparison) show specific peaks and shape that characterize each system and differentiate the spectra according to the spin and charge state. The Raman spectra of the NV^0 defects shows a single peak, redshifted with respect to the single peak of pristine diamond by 2 cm^{-1} only, but in turn well separated from the negatively charged form of the defect.

1. Introduction

Despite the strength of the C–C bond, the diamond lattice contains a large number of point defects. Nitrogen is the most abundant extrinsic impurity in diamond; nitrogen-contained diamonds are classified into the types *Ia* and *Ib*. In *Ib* diamond, isolated nitrogen atoms substitute single carbon atoms [1,2], leading to the so-called substitutional defects, N_s. For *Ia* type, the lattice contains aggregates of nitrogen atoms, mostly vicinal N_s pairs, known as A and B aggregates; in the latter four N_s surround a carbon vacancy [3,4]. Pure natural *Ib* diamonds are extremely rare, because high geological temperatures and pressures promote aggregation. On the contrary, synthetic diamonds produced by CVD (chemical vapour deposition) and controlled HTHP (high temperature high pressure) grow generally as type *Ib*, with even the desired concentration of N_s [5].

Diamond, with its high melting point, chemical stability, wide band gap, high carrier mobility and optical transparency in the Infrared (IR), is an attractive candidate for application in numerous areas of technological importance, including high temperature diodes, microwave transistors, thermistors and radiation detectors [6,7]. All relevant technological applications are in general related to the presence of intrinsic and extrinsic defects characterizing both natural and synthetic diamond [8–13], and for this reason they have been the subject of theoretical and experimental investigations [10–23].

Between the available experimental techniques, the IR and Raman spectroscopies are generally applied for elucidating the vibrational

* Corresponding author.
** Corresponding author.
E-mail addresses: anna.ferrari@unito.it (A.M. Ferrari), maddalena.damore@unito.it (M. D'Amore).

https://doi.org/10.1016/j.jpcs.2021.110304
Received 17 June 2021; Received in revised form 28 July 2021; Accepted 31 July 2021
Available online 9 August 2021

behaviour of different defected diamond lattices, that frequently allow to identify the fingerprints of various point-defects in both natural and synthetic diamond and in diamond-like materials [11,12,17,21,22,24–30].

For open-shell defects, Electron Paramagnetic Resonance (EPR) and Electron Nuclear Double Resonance (ENDOR) spectroscopies have been shown to be powerful tools for establishing the spin/charge state of the defects and their local symmetry [31,32].

Ib diamonds subjected to neutron (or radiative) damage and annealing show sharp absorption and very intense photoluminescence peaks at 638 and 575 nm (1.945 and 2.156 eV) whose intensity correlates with the neutron dose and with the intensity of carbon vacancy GR1 signal in addition with a ^{15}N isotopic shift of the vibronic side bands. The defect has been indeed identified as formed by a vacancy and a substitutional N, the NV defect. Photoconversion experiments have assigned the 638 and 575 nm peaks at the same defect but in different charge states, NV^- and NV^0, respectively. Confirmation of the nitrogen-vacancy structure with a trigonal symmetry and the proposal of a negative charge with a triplet spin state has been first provided by Loubser and van Wyk [32,33] through their observation and interpretation of an EPR signal correlated with the NV^- optical band. The model has been supported by cluster and periodic *ab initio* calculations and sophisticated experiments (see Ref. [31] for a review). It was more difficult to establish the spin multiplicities of the NV^0 ground state because of the long absence of any EPR observation to be correlated to the NV^0 optical band; that allowed only speculations on a spin doublet ground state whose EPR signal was undetectable because of a dynamical Jahn–Teller effect [34], previously observed by Davies [35]. Only the relatively recent detection of a metastable spin quartet EPR signal [34] has finally dissolved the doubts on that topic: the EPR signal is consistent with the a spin doublet ground state for NV^0.

Over the last five decades the interest of researchers has been mainly devoted to the study of NV^- due to a number of applications of that system [36–40]. However, starting from the observation of the EPR activity of NV^0, that centre found a renewed interest *per se*, due to the glimpsed applicative potentialities and not only as a reference for the NV^- defect.

The present paper reports new calculations of the charge and spin density, band structure, IR and Raman spectra and hyperfine coupling constant of the NV^0 defect in diamond lattice. Both the doublet ($S_Z = 1/2$) and the spin excited quadruplet ($S_Z = 3/2$) states have been investigated. To take into account the Jahn–Teller effect occurring in the $S_Z = 1/2$ NV^0 (NV^0_d) the symmetry of the centre has been reduced to C_S, while for the $S_Z = 3/2$ NV^0 (NV^0_q) the trigonal symmetry C_{3v} has been retained.

2. Computational models and details

DFT [41,42] calculations reported in this paper were based on the B3LYP global hybrid functional [43,44], as implemented in the CRYSTAL program [45,46]; however, selected features of the electronic properties of the NV^0 defect have also been examined by using other DFT formulations based on pure LDA [47,48] and PBE [49], and the global PBE0 [50] and range-separated HSE06 [51] functionals. Pople's standard 6-21G [52] *all-electron* basis sets of Gaussian type functions have been adopted for both carbon and nitrogen, except for values of 0.23 and 0.30 $Bohr^{-2}$ for the exponents of the outermost *sp* shells of the host and dopant atoms, respectively. For checking the reliability of our results, two sets of additional basis sets have been adopted. The 6-21G* and 6-31G* basis sets have been used to test the formation energy of the NV^0 defect, along the same lines used for the calculation of the properties of other nitrogen defects (see for instance Refs. [54,55]). The second set consists in the 6-31G-J* bases [56] used to compute the electron-nuclear spin hyperfine coupling tensor; this set was specifically designed for calculating spin coupling constants by means of small but, sufficiently accurate, basis sets. The 6-31G-J* bases were derived from the standard 6-31G basis set by expanding the core functions followed by a new contraction of the valence functions [56], resulting in a 811111-41-1 → [5s,2p,1d] basis, improperly referred to as a 6-31G type. Hyperfine coupling constants have been calculated at the B3LYP/6-31G-J* level, with a S_{216} supercell. In a previous report (see Ref. [55]), the B3LYP/6-31G-J* combination has been found to compute Fermi contact terms in excellent agreement with the corresponding experimental values; in this regard, the 6-31G-J* basis set turned out to be a good compromise between accuracy and computational affordability. In addition, the size of the adopted supercell has been shown to be large enough to correctly account for hyperfine coupling constants at the peripheral sites and to provide values actually indistinguishable from those computed with larger supercell [55]. PBE/6-31G-J* have also been considered for comparison with previous calculations.

Other details on the computational set up and the calculation of the vibrational frequencies and the hyperfine coupling tensor (HF), are collected in the Supplementary Information section.

3. Results

The B3LYP geometry and the atomic charges, atomic magnetic moments and bond populations as resulting from a Mulliken analysis of the charge and spin density of the S_{216} supercell are shown in Fig. 1. The substitution by nitrogen of a single carbon adjacent to the vacancy reduces the symmetry from tetrahedral, T_d (24 operations) to trigonal, C_{3v} (6 symmetry operations); nitrogen is covalently bound to three of the four nearest-neighbour carbon atoms ($C_{(b)}$ in Fig. 1), as the lone pair prevents the formation of a fourth bond. The nitrogen lone-pair points along the C_{3v} axis, towards the three carbon atoms adjacent to the vacancy ($C_{(c)}$ in Fig. 1) each one possessing a singly-occupied 'dangling' bond. The possible spin states are then a quadruplet q ($S_z = 3/2$, three α electrons) corresponding to the $(a_1)^1e^2$ configuration ($^4A_2$ electronic state, the NV^0_q system) and a doublet d ($S_z = 1/2$, two α and one β electrons) corresponding to the $(a_1)^2e^1$ configuration (^2E electronic state), see Figs. S1 and S2 of the Supplementary Information. In the latter configuration a single electron occupies a double degenerate level yielding to a Jahn Teller (JT) distortion that allows to remove the degeneracy and to lower the total energy. The symmetry reduces from C_{3v} to C_S and the double degenerate e band splits in $a' \oplus a''$. The process

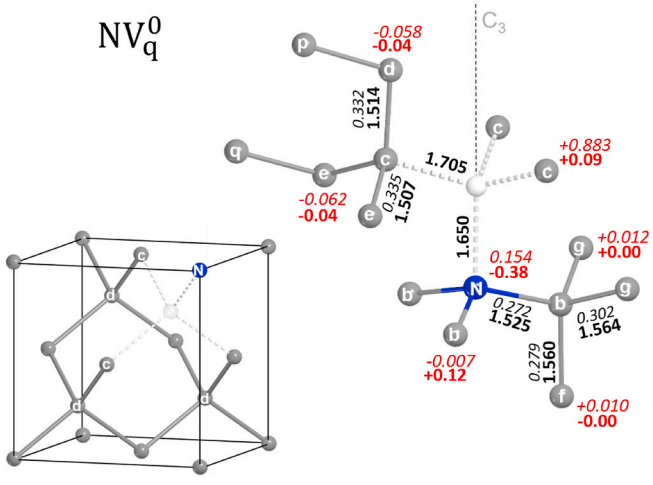

Fig. 1. Atomic distances (**bold**, black), bond populations (*italic*, black), atomic charges (**bold**, red), and atomic magnetic moments (*italic*, red) as resulting from a Mulliken analysis are reported. Mulliken data in $|e|$, distances in Å. The distances and bond populations appear below the bonds, net charges and magnetic moments close to the atomic positions. Data refer to the quadruplet (NV^0_q, $S_z = 3/2$) solution, whose symmetry is C_{3v}. Data refer to calculations performed with the S_{216} supercell, the B3LYP functional and the 6-21G basis set.

leads to two different electronic configurations and corresponding electronic states: $(a')^2(a')^1$ ($^2A'$, the NV^0_{d1} system) and $(a')^2(a'')^1$ ($^2A''$, NV^0_{d2}) both relevant in determining the effective JT potential (that will be discussed in a forthcoming paper) and indeed both analysed here in details.

3.1. Geometry, charge and spin densities and band structure

3.1.1. The quadruplet $S_z = 3/2$

We first discuss the NV^0_q system. The N atom and the three $C_{(c)}$ bearing the three unpaired electrons are pushed away from the vacancy site, located at the geometrical centre of the four neighbouring atoms (the V–N and V–$C_{(c)}$ distances are 1.650 and 1.705 Å) because of the strong repulsion between the nitrogen lone pair and the 'dangling' bonds. The three N–$C_{(b)}$, the three $C_{(c)}$-$C_{(d)}$ and the six $C_{(c)}$-$C_{(e)}$ bond lengths reduce from 1.560 Å (in perfect diamond) to 1.525, 1.514 and 1.507 Å, respectively (see Fig. 1). Such a lattice deformation decays rapidly, so that, starting from $C_{(c)}$, bond distances involving second neighbour, $C_{(e)}$-$C_{(q)}$ and $C_{(e)}$-$C_{(i)}$ or $C_{(d)}$-$C_{(h)}$ and $C_{(d)}$-$C_{(p)}$ are ~ 1.56 Å, and similarly, starting from N, $C_{(b)}$-$C_{(f)}$ and $C_{(b)}$-$C_{(g)}$ are 1.560 and 1.564 Å, respectively; these values are negligibly larger than in perfect diamond lattice, see Fig. 1.

The net charges resulting from a Mulliken population analysis (see Fig. 1) are −0.38 $|e|$ on N, +0.12 $|e|$ on $C_{(b)}$, whereas the second neighbour carbon atoms are essentially neutral. Similarly, the Mulliken populations on $C_{(c)}$ and on $C_{(d)}$ and $C_{(e)}$ (first neighbours to $C_{(c)}$) are +0.09 $|e|$ and −0.04 $|e|$ and zero for farther neighbours. The N–$C_{(b)}$ bond population is +0.272 $|e|$, which is not too far from the corresponding C–C value in perfect diamond (+0.305 $|e|$). The N–C bond population is about the same as for C–C: the shorter distance compensates the less covalent character of the bond as a result of its partial ionic nature. The bond population of the $C_{(c)}$-$C_{(d)}$ and $C_{(c)}$-$C_{(e)}$ bond (the distances are shorter than in pure diamond) is larger than in diamond (+0.335 $|e|$) as a consequence of the reduced coordination of $C_{(c)}$ (the $C_{(c)}$ charge is almost negligible).

The spin density is largely localised at the defect site on the three carbon atoms facing the vacancy ($C_{(c)}$, +0.883 $|e|$), and propagates along the bonds in a smoothly damped way with non negligible values up to several shells of neighbours. Thus, from N outwards, the value of the spin density is 0.154, −0.007, 0.010 and 0.012 $|e|$ on N, $C_{(b)}$, $C_{(f)}$, and $C_{(g)}$, respectively. From $C_{(c)}$ outwards, +0.883, −0.058, −0.062, −0.036 and 0.012 $|e|$ on $C_{(c)}$, $C_{(d)}$, $C_{(e)}$, $C_{(q)}$, and $C_{(h)}$ (see Figs. 1 and 2).

The band structure of NV^0_q, obtained from a S_{216} supercell, is shown in Fig. 3. The three unpaired electron occupied bands are of α type, whereas the empty ones are of β type: the first occupied level (a_1 symmetry) is just 0.46 eV above the top of the valence band (VB), and 0.66 eV (in Γ) below the two other defect levels (e), fully degenerate in Γ. The band gap values along the α and β channels, $E^\alpha_g = 4.87$ and $E^\beta_g = 2.64$ eV (B3LYP values), are only marginally affected by the computational conditions, adopted hybrid functional and basis set. However, when the gradient corrected PBE functional is used, the gaps are considerably smaller, up to 2 eV, and no gap exists in LDA for NV^0_q (see Table 1). The main gap, the energy difference between the top VB and the bottom CB (conduction band), E_g = 5.83 eV (B3LYP), is actually the same as in pristine diamond, whose gap is estimated at E_g = 5.85 eV; the latter value, predicted by our simulation, is in good agreement with both the measured value of 5.4–5.6 eV [57,58], and the value extrapolated to 0 K by Cardona (5.80 eV) [59].

3.1.2. The doublet $S_z = 1/2$

We turn now to the two different doublet states, NV^0_{d1} and NV^0_{d2} whose structures are sketched in Figs. S1 and S2 of SI. In order to label the atoms in the C_S low symmetry, that in the high symmetry belong to the same shell of neighbours, the same label has been used, adding a superscript (') and (") if necessary. Thus, for instance the 3 $C_{(c)}$ in C_{3v}, become 1 $C_{(c)}$ and 2 $C_{(c')}$ in C_S; the 6 C_{3v} $C_{(g)}$ transform in 2$C_{(g)}$, 2$C_{(g')}$, and 2 $C_{(g'')}$ in C_S and so on, see Table S1 of SI for a complete list.

The JT distortion leads to non equivalent V–C distances: in NV^0_{d1} the bond is compressed when lying in the mirror plane, V–$C_{(c)}$ = 1.642, and elongated outside the plane V–$C_{(c')}$ = 1.678 Å; conversely in NV^0_{d2} the bond is stretched when lying in the mirror plane, V–$C_{(c)}$ = 1.700, and

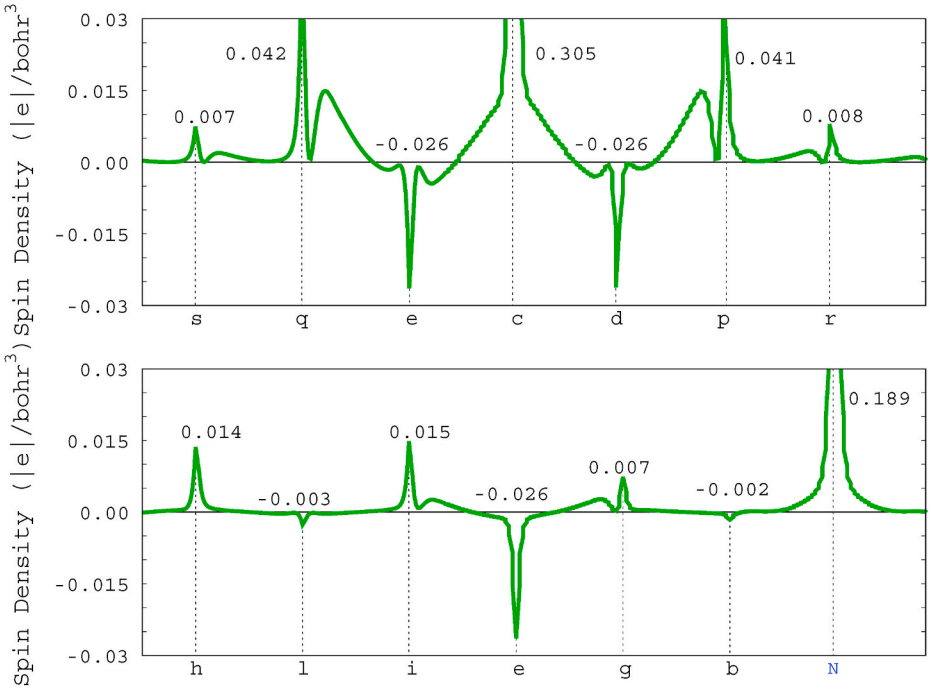

Fig. 2. Spin density profile of the NV^0_q defect along various paths. See Fig. 1 for the labels of the atoms. Centers r, s, h, i, not shown in Fig. 1, are first neighbours of carbons p, q, d and e, respectively; center l is bound to carbons h and i. See also Fig. S3 of the Supplementray Information section for a complete labeling of the atoms. Calculations performed with the S_{216} supercell, B3LYP functional and 6-21G basis set.

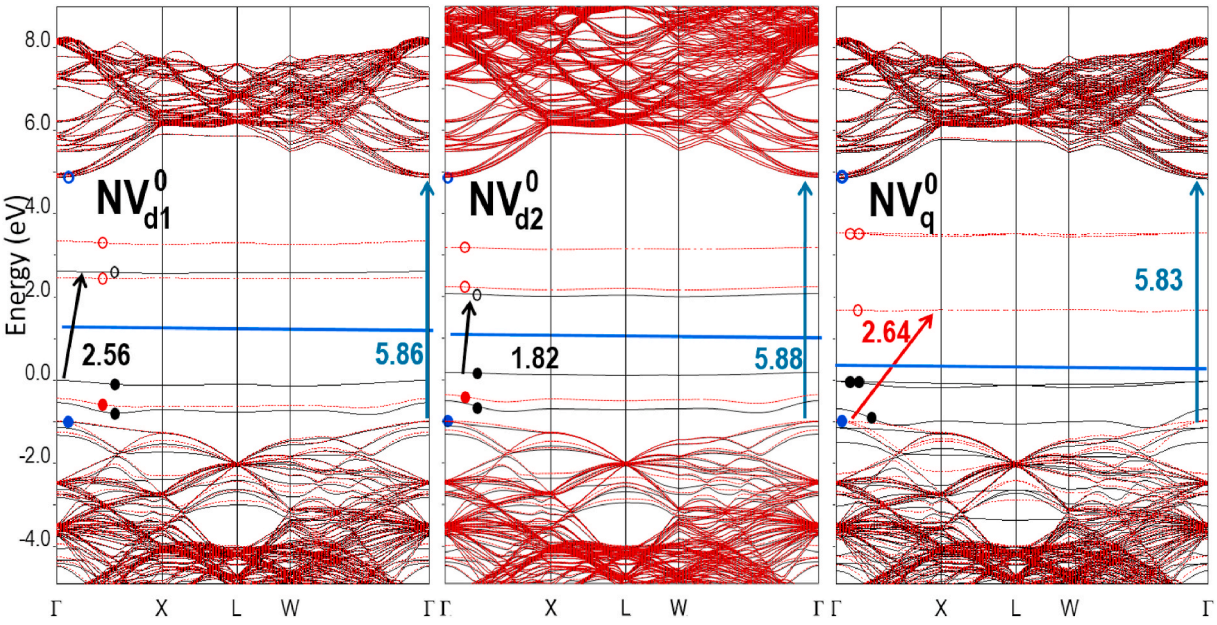

Fig. 3. Band structures of the NV^0 defect in the doublet ($S_z = 1/2$) ground (left) and excited (center) electronic state, and of the quadruplet ($S_z = 3/2$, right). computed with a S_{216} supercell, B3LYP functional and 6-21G basis set. Filled (empty) dots indicate occupied (virtual) defect states. Black and red dots identify α and β bands.

Table 1
Energy data of the NV^0 defect obtained with different methods and basis sets. E_g^α and E_g^β are the energy gaps for α- and β-electrons, respectively. E_f is the formation energy of the defect as obtained from Equations (1) and (3). ΔE_S is the energy difference between the doublet (ground state) and quadruplet spin states. E_g^{Pure} is the gap of pure diamond. Best estimate of experimental E_g^{Pure} is 5.80 eV from Ref. [59] (see text for details). All data are in eV.

Method	Basis Set	NV^0_q		NV^0_{d1}		NV^0_{d2}		E_g^{Pure}		ΔE_{d1-q}	ΔE_{d1-d2}	E_f^1		E_f^2	$E_f^{NV^0}$
		E_g^α	E_g^β	E_g^α	E_g^β	E_g^α	E_g^β								
B3LYP	6–21	4.87	2.64	2.56	2.82	1.82	2.52			5.56	0.46	0.23	5.85	15.72	−4.59
	6-21*	4.91	2.59	2.49	2.81	1.78	2.52			5.75	0.49	0.21	5.81	15.47	−4.63
	6-31*	4.98	2.66	2.55	2.86	1.79	2.55			5.91	0.47	0.22	5.68	15.10	−5.14
PBE0	6–21	5.14	2.96	3.05	3.23	2.29	2.95			5.80	0.47	0.24	5.92	16.92	−4.71
HSE06	6–21	4.43	2.33	2.32	2.55	1.60	2.29			5.17	0.47	0.22	5.90	16.89	−4.70
PBE	6–21	2.92	1.28	0.62	1.30	0.40	1.16			4.09	0.59	0.05	5.57	16.39	−4.36
LDA	6–21	–	–	0.29	1.23	0.26	1.18			4.03	0.08	0.01	5.23	17.97	−4.55

squeezed outside the plane, $V–C_{(c')} = 1.589$ Å. The three $C_{(c)}$ atoms form an isosceles triangle with θ (the angle bisected by the mirror plane) equal to 62° in the former case and $\theta = 58°$ in the latter one. The alternation of shorter and longer bond distances propagates outside the defect site but rapidly relax to the perfect diamond values, as for NV^0_q.

The net charges are quite similar in the two systems: they are −0.41 |e| on N, ∼ +0.09 |e| on $C_{(b)}$ and $C_{(b')}$ for NV^0_{d1}; −0.38 |e| on N, ∼ +0.13 |e| on $C_{(b)}$ and $C_{(b')}$ for NV^0_{d2}. As for NV^0_q, the other carbons are essentially

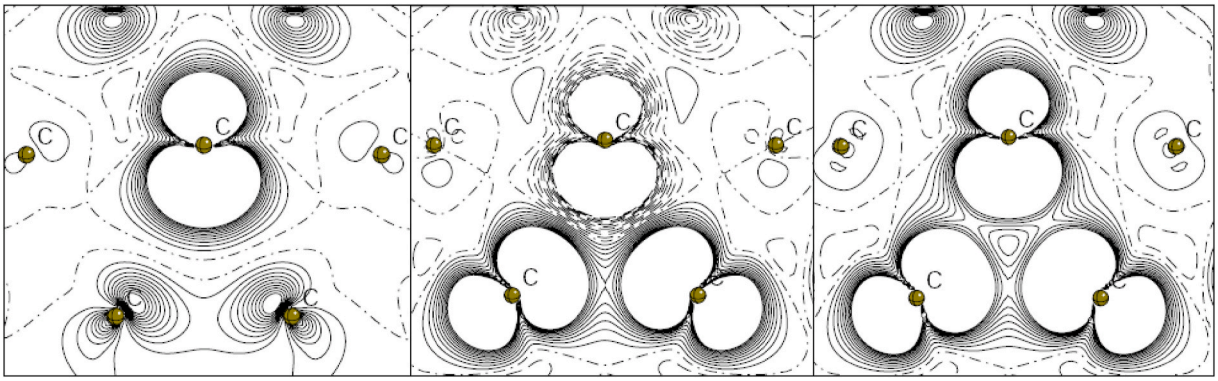

Fig. 4. Spin density maps of the NV^0 defect in the doublet ($S_z = 1/2$) ground (left) and excited (center) electronic state, and of the quadruplet ($S_z = 3/2$, right). The plane of the figure is defined the three carbon atoms sitting on the border of the vacancy. Isodensity lines differ by 0.01 |e| ($bohr^3$); spin density is truncated at ± 0.1 |e| ($bohr^3$). Continuous, dashed and dot-dashed black lines indicate positive, negative and zero values, respectively.

neutral.

Unlike charges, the spin distributions in the two doublet states are extremely different. The atomic momentum μ is: $C_{(c)}$, +0.800, $C_{(c')}$, −0.679, N, +0.020 $|e|$ for NV^0_{d1}; $C_{(c)}$,+0.044, $C_{(c')}$, +0.855, N, +0.006 $|e|$ for NV^0_{d2}. In both cases the μ value on N is quite small. The spin density is mainly localised at the carbon atoms adjacent the vacancy site; it propagates however through bonds as discussed for NV^0_q, see also Fig. 4.

The band structure of NV^0_{d1} and NV^0_{d2} are very similar both in the valence and virtual manifold. Two of the occupied defect levels are nearly degenerate (one α and one β), and appear, at the Γ point, at 0.46 (0.54) eV and at 0.50 (0.63) eV for NV^0_{d1}(NV^0_{d2}) above the top of the valence band; the third one, α, is located at about 0.53 (NV^0_{d1}) and 0.68 (NV^0_{d2}) eV above the latter one. The main difference between the two doublets is in the gap among the occupied and empty defect levels, that is 2.56 eV in NV^0_{d1} and reduces to 1.82 eV in NV^0_{d2}.

3.2. Energetics: relative stability of NV^0 states and formation energy

NV^0_{d1} is the ground state of the NV^0 system; with respect to it, NV^0_{d2} and NV^0_q correspond respectively to the lowest spin forbidden and spin conserved excited electron states. NV^0_{d1} is more stable than NV^0_q, ΔE_{d1-q} ∼ 0.5 eV, and NV^0_{d1} more stable than NV^0_{d2}, ΔE_{d1-d2} ∼ 0.2 eV, irrespective to the functional or basis set employed in the calculation (the only exception is PBE that provides ΔE_{d1-d2} estimates significantly lower than the corresponding values from hybrid functionals and from LDA, that however describes NV^0_q as a conductor), see Table 1.

The formation energy of a defect (E_f) is usually defined as

$$E^i_f = (E_P - n \cdot E^i_C) - (E_D - m \cdot E^i_N) \quad (1)$$

where E_P and E_D are the total energies of the pristine and defective diamond supercells, and E^i_C and E^i_N are the energies of the single carbon and nitrogen atoms, respectively; n is the number of carbon atoms eliminated, and m the number of nitrogen atoms added in the unit cell (in the present case $n = 1$ and $m = 1$). The superscript $i = 1, 2$ indicates two different ways to calculate the atomic energies. For $i = 1$, E^i_N and E^i_C are half of the total energy of the N_2 molecule for nitrogen and the energy of a single carbon atom in the pristine diamond structure, whereas for $i = 2$ they are the energies of the isolated atoms. Table 1 contains formation energies computed with various functionals, from PBE0 to LDA, and basis sets, from 6-21G to 6-31G*. It shows that, with the exception of LDA, all functionals provide formation energies that differ by less than 0.4 eV, and that the use of larger basis sets such as 6-31G* can affect E^1_f and E^2_f by up to ∼0.4 and ∼1.2 eV, respectively.

In diamond, NV defects are formed through a process of radiative damage that promote the formation of the carbon vacancies, followed by annealing that increases their mobility, according to the reaction:

$$N_s + V_0 \rightarrow NV^0 \quad (2)$$

(a neutral vacancy has been considered in this case) with a corresponding formation energy

$$E^{NV^0}_f = (NV^0 - N_S - V^0). \quad (3)$$

$E^{NV^0}_f$ is always negative, about −4.5 eV, irrespective to functional or basis set adopted in the calculation, see Table 1. The result undoubtedly indicates that the process of aggregation between a mobile vacancy and a substitutional nitrogen yielding to the formation of a NV^0 defect is exothermic, as expected.

3.3. The Infrared and Raman vibrational spectra

The IR and Raman spectra of pristine diamond are very simple: the former, due to symmetry, is completely flat (no peaks) so that any additional peak is due to defects; the latter is characterized by a single peak at 1332 cm^{-1} (the calculated one with the present functional and basis set is at 1317 cm^{-1}, 15 cm^{-1} below the experiment). IR and Raman spectra of the of NV^0 defects (NV^0_{d1}, NV^0_{d2} and NV^0_q) are reported in Fig. 5 and 6. For comparison, the spectra of NV^- (the charged state of NV^0) are also reported, since it can be of interest to see how different charge (and then electronic and spin) states can affect the vibrational features (a detailed analysis of the electron structure of this defect computed at the same level of theory can be found in Ref. [60,61]).

The Raman spectra of NV^0 defects remains very similar to the pure diamond one: a single sharp peak at 1315 cm^{-1} (then just 2 cm^{-1} below the peak of pure diamond), irrespective of the spin state of the defect; the rest of the 400–1315 cm^{-1} windows is essentially empty (peaks appear in the background, that have intensity 3 to 4 orders of magnitude lower

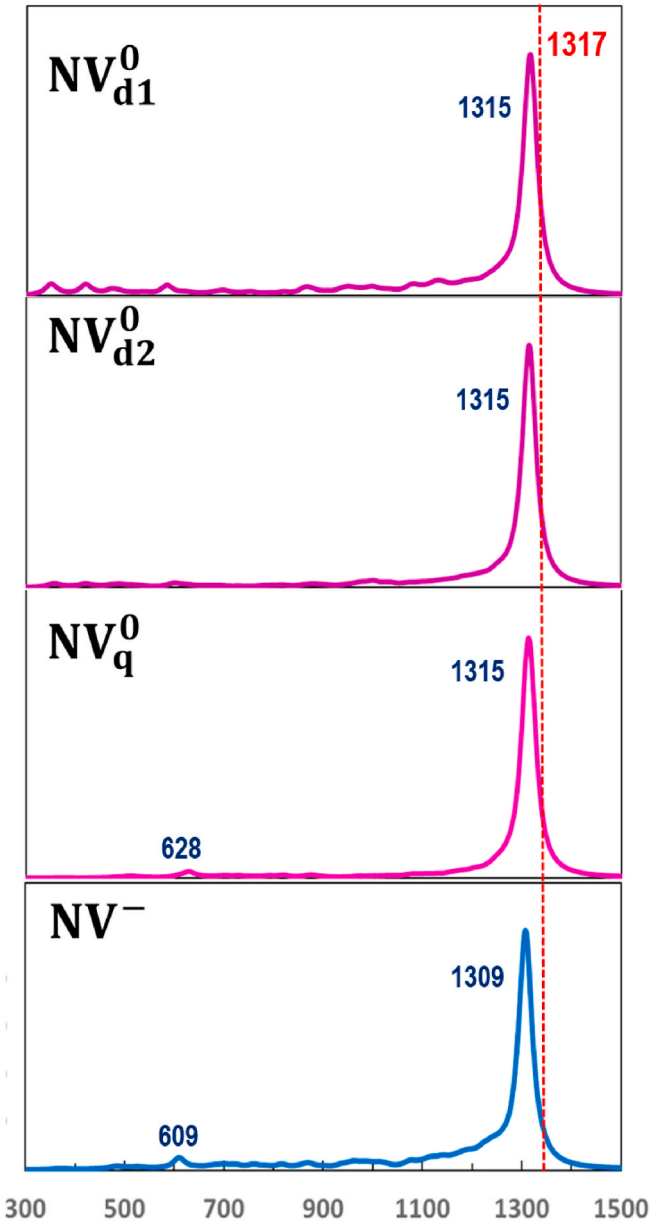

Fig. 5. The Raman spectra for the *quadruplet* NV^0_q and the two different *doublet* states: NV^0_{d1} and NV^0_{d2} of the NV^0 defect in diamond. The spectra of the NV^- *triplet* state is reported for comparison. The vertical dotted lines indicate the Raman peak of pristine diamond. A Lorentzian convolutions of 30 cm^{-1} has been adopted for all spectra. Intensity are in arbitrary units to favor comparison among spectra.

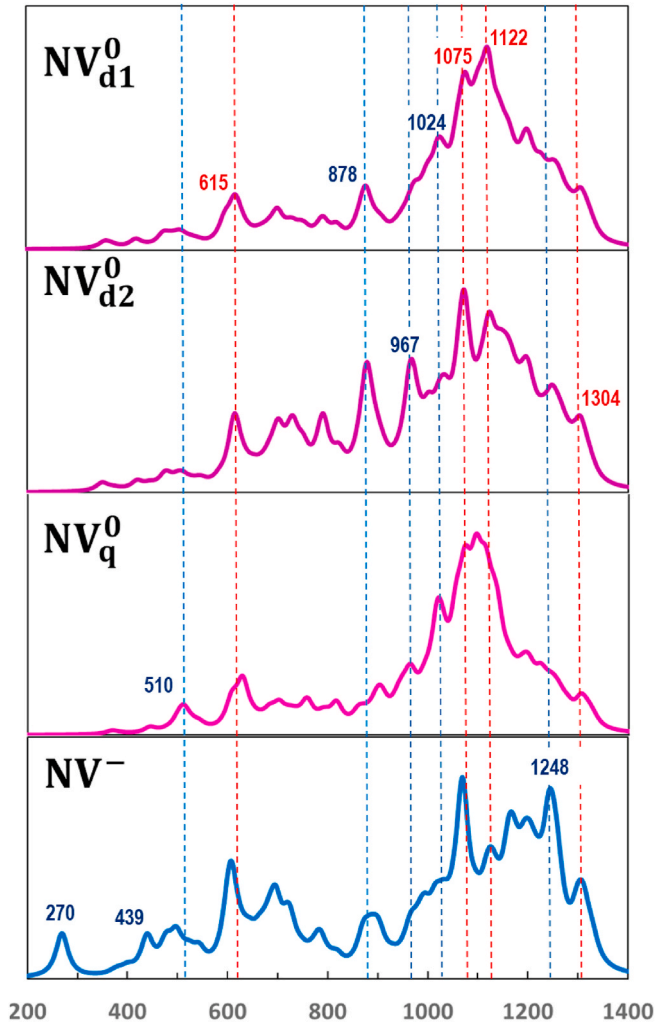

Fig. 6. The IR spectra for the *quadruplet* NV^0_q and the two different *doublet* states: NV^0_{d1} and NV^0_{d2} of NV^0 defect in diamond. The spectra of the NV^- *triplet* state is reported for comparison. The vertical dotted lines indicate the most relevant peaks; red lines indentify peaks common to all four systems. A Lorentzian convolutions of 30 cm^{-1} has been adopted for all spectra. Intensity are in arbitrary units to favor comparison among spectra.

than the one at 1315 cm^{-1}, see Fig. 5. In the Raman spectrum of the NV^- defect, the single, dominant peak is at 1309 cm^{-1}, (then just 8 cm^{-1} below the peak of pure diamond). So the main difference with respect to pristine diamond is observed for NV^-, and is not due to the presence of N, but to the negative charge.

The IR spectra of the NV defects, span the ~ 300 cm^{-1} to 1340 cm^{-1} interval (just 23 cm^{-1} above the calculated Raman peak of pristine diamond); the 3M − 3 (M = 215) modes form nearly a continuum, with no peaks protruding from the *perturbed diamond* manifold as is the case of other diamond defects containing heteroatoms (see for instance Ref. [53]). The spectra show however specific features that deserve some comments. We start with the ground state system, NV^0_{d1}. The IR spectrum is dominated by two intense peaks at 1075 and 1122 cm^{-1}; less intense signals appear at 615, 878, 1024 (with a shoulder at 967), 1195 and 1304 cm^{-1}. In the case of NV^0_{d2} we observe the same modes, but with important differences in intensity. The two main peaks at 1075 and 1122 cm^{-1} still dominate the spectrum but with reversed intensities; the shoulder at 967 cm^{-1} and the peaks at 615 and 878 cm^{-1} are now of medium and comparable intensities. The two spectra differ remarkably in their overall shape: narrow and centred at 1075 cm^{-1} the former, very widened and centred at 1075 cm^{-1} the latter one. The IR spectrum of NV^0_q seems very similar to that of NV^0_{d1}, but with important differences: compared to NV^0_{d1}, the very intense central peak that dominates the spectrum is narrower and centred at about 1080 cm^{-1}; the 876 band is not present; the signal at 615 cm^{-1} is shifted at 628 cm^{-1} and is accompanied by a weaker peak at 510 cm^{-1}.

Finally we analyse how the IR spectrum changes if the defect becomes negatively charged. For NV^- the spectrum is dominated by two major peaks at 1069 and 1248 cm^{-1}, with additional strong signals in between at 1125, 1166 and 1194 cm^{-1}. The band at 1069 cm^{-1} is common to all four defects (even if downshifted by ~ 6 cm^{-1} in NV^- with respect to NV^0_{d1}), while that at 1248 cm^{-1} is specific for NV^-. Less intense peaks (medium) appear at 270, 439, 608, 696, 878 and 1304 cm^{-1}; the signals at 270 and 439 are not observed in neutral defects and the 608 cm^{-1} peak is at 615 cm^{-1} in NV^0_{d1}. Thus, the shape of the spectrum appears quite different from the NV^0 cases, see Fig. 6.

Isotopic substitutions have been used in the attempt to identify *defect-like* modes, that is, modes in which N displacements are involved to a larger extent in the definition of the normal coordinate. The $^{14}N \rightarrow ^{15}N$ isotopic substitution causes an isotopic shift larger than 5 cm^{-1} in only one mode that is present in all the four systems. Analysis of the corresponding normal coordinates reveals that these modes are out of plane displacements (umbrella like motion) of the N–C trigonal unit coupled with a similar motion of the $C_{(c)}$-C (or $(C_{(c')})$ trigonal units centred at the carbon atoms facing the vacancy. These modes contribute to define the peaks at ~ 615 cm^{-1} (NV^0_{d1} and NV^0_{d2}), at 628 cm^{-1} (NV^0_q) and at 608 cm^{-1} (NV^-) that despite the relatively low intensity appear to be well identifiable in that spectral region and therefore can comfortably be related to the presence of NV defects. In addition, the significant shift with respect to the two doublets, towards higher wavenumbers (13 cm^{-1}) in NV^0_q and to lower wavenumbers (10 cm^{-1}) in NV^-, can help to identify defects in different spin and charge states.

3.4. The hyperfine coupling tensor

EPR data are available only for the spin excited quadruplet state, while for the doublet ground state the HF coupling has not been measured due to the dynamic JT effect (see Ref. [62] for a recent discussion). For NV^0_q, the experimental hyperfine coupling values, A_{iso} and B_1, B_2 and B_3, are scarce. The only set of data we have been able to find refers to the *central* N atom, in its isotopic form ^{15}N [34]. Also on the simulation side there is only one set of data, reporting the hyperfine coupling data for ^{15}N and for $^{13}C_{(c)}$, the first neighbour of the vacancy [63]. These data are reported in Table 2. The labels *a*, *b*, *c*,..,given in brackets in Table 2 are the same as in Fig. 1, (see also Fig. S3 and Table S1 of Supplementary Information for a complete list). Subscripts, 1,2 …., label the absolute values of A_{iso} in decreasing order. All values larger than 2 MHz are shown.

Fig. 2 shows that the spin density in NV^0_q is very high on the three $C_{(c)}$ atoms, and at the N site (see also the atomic magnetic moments in Fig. 1. Note however that the spin density is small, but but non-negligible on many atoms far from the defect region. The second and third largest spin density (then C_2 and C_3 in Table 2) are on the *p* and *q* atoms, a result somehow surprising, as they are NOT the 1st and 2nd neighbours of $C_{(c)}$ (*d* and *e* are such neighbours). Bower and Symons [64] have proposed an explanation for this feature through a mechanism similar to hyperconjugation, taking place through bonds, in which the electron density at (p) and (q) are enhanced by the relatively large *p*-electron population at $C_{(c)}$ (note the large components of the $\mathcal{B}$ tensor at this site), see Table 2. Actually sites (d) and (e) are directly bound to $C_{(c)}$, and (p) and (q) are bound to (d) and (e).

The Mulliken analysis, reported in Table S1 of the Supplementary Information section, is not able to correctly represent the behaviour of spin density. Alternative interpretation schemes are available in the literature (see for instance Refs. [65–69]), and among them the Bader

Table 2
B3LYP and PBE computed hyperfine coupling constants (in MHz) for the NV_q^0 defect ($S_Z = 3/2$, M = 4). The 6-31-J* basis set has been used. Values are for S_{216} supercells with the geometry optimized at the B3LYP/6-21G computational level. The labels in round brackets are those shown in Fig. 1. Experimental values are from Felton Ref. [34], calculated values from Gali [63] who adopts a method whose ingredients are PAW (Projected-Augmented-Wave), PW (plane waves), Local Spin Density Approximation (LSDA).

		Method	A_{iso}	B_1	B_2	B_3
^{14}N		B3LYP	20.05	−2.75	−2.75	5.50
		PBE	20.51	−3.05	−3.05	6.10
^{15}N		B3LYP	−28.12	−7.71	3.86	3.86
		PBE	−28.76	−8.55	4.28	4.28
		Exp.	−27.77	−7.93	3.97	3.97
		Calc.	−28.60	−10.40	5.20	5.20
$^{13}C_1$	(c)	B3LYP	82.12	−24.61	−24.45	49.06
	(c)	PBE	71.05	−22.40	−22.30	44.70
	(c)	Calc.	82.60	−21.60	−22.00	43.60
$^{13}C_2$	(q)	B3LYP	12.58	−1.84	−1.69	3.53
	(q)	PBE	11.76	−1.81	−1.63	3.44
$^{13}C_3$	(p)	B3LYP	12.35	−1.84	−1.72	3.56
	(p)	PBE	11.44	−1.81	−1.63	3.44
$^{13}C_4$	(d)	B3LYP	−6.60	−1.19	−0.81	2.00
	(d)	PBE	−5.42	−1.25	−0.73	1.98
$^{13}C_5$	(e)	B3LYP	−6.60	−0.99	−0.62	1.60
	(e)	PBE	−5.23	−1.04	−0.52	1.56
$^{13}C_6$	(i)	B3LYP	4.37	−0.87	0.07	0.80
	(i)	PBE	4.01	−0.83	0.11	0.72
$^{13}C_7$	(h)	B3LYP	4.00	−0.31	−0.09	0.41
	(h)	PBE	3.70	−0.78	0.06	0.72
$^{13}C_8$	(r)	B3LYP	2.35	−0.47	−0.38	0.85
	(r)	PBE	2.48	−0.48	−0.41	0.89

spin populations account well for this effect and excellently reproduce the spin density profile of Fig. 2, see Table S1 of SI. According to the spin profile, $\mu = -0.026$ $|e|$ at sites $C_{(d)}$, $C_{(e)}$, and $\mu = 0.041$ and 0.042 $|e|$ at sites $C_{(p)}$, $C_{(q)}$. The Bader analysis provides similar results: $\mu = -0.003$ and -0.007 $|e|$ at sites $C_{(d)}$, $C_{(e)}$, and $\mu = 0.042$ and 0.043 $|e|$ at sites $C_{(p)}$, $C_{(q)}$.

As expected, C_4 and C_5 correspond to $C_{(d)}$ and $C_{(e)}$, with a change of sign in the spin density, and C_6 and C_7 to $C_{(i)}$ and $C_{(h)}$, (respectively bound to $C_{(e)}$ and $C_{(d)}$). Finally C_8 correspond to $C_{(r)}$ and not to $C_{(l)}$, although they are 24th and 5th neighbour from $C_{(c)}$, but respectively bound to $C_{(p)}$ and to $C_{(h)}$. Spin profile ($\mu = 0.008$ and -0.003 $|e|$ at sites $C_{(r)}$ and $C_{(l)}$) and Bader spin population ($\mu = 0.0072$ and -0.0020 $|e|$ at sites $C_{(r)}$ and $C_{(l)}$) supports this correspondence. As a final remark, we underline that sites $C_{(b)}$ and $C_{(g)}$, respectively 1st and 2nd neighbours of N are not present in the list of the eight largest values of A_{iso} (or of the spin density at the atomic positions).

The B3LYP/6-31G-J* results are in excellent agreement with the only experimental data available for ^{15}N [34]. Our A_{iso} value differs from the observed one by less than 2 % and the agreement is even better for the components of the $\mathcal{B}$ tensor, as Table 2 confirms. With respect to previous calculations, the agreement for both the ^{15}N and $C_{(c)}$ centers is good.

The computed $\mathcal{A}$ tensor of N and $C_{(c)}$ for the NV_{d1}^0 and NV_{d2}^0 defects are also reported in Table S2 of SI, even if experimental data are not available.

4. Conclusions

The structural, electronic and magnetic properties of the NV^0 defect in diamond have been investigated by means of a supercell approach through DFT methods. The possible spin states of NV^0 are a quartet NV_q^0 ($S_z = 3/2$, three α electrons corresponding to the electron configuration $(a_1)^1e^2$ ($^4A_2$ electronic state, the NV_q^0 system) and a doublet d corresponding to the $(a_1)^2e^1$ configuration (^2E electron state). In the latter configuration a single electron occupies a twofold degenerate level yielding a Jahn Teller distortion that removes the degeneracy and lowers the total energy. The point symmetry reduces from C_{3v} to C_S and the double degenerate e band splits in $a' \oplus a''$. Two local minima are localized corresponding to the electronic states: $(a')^2(a')^1$ ($^2A'$, the NV_{d1}^0 system) and $(a')^2(a'')^1$ ($^2A''$, NV_{d2}^0). In the two cases the V–C distance is different: in NV_{d1}^0 it is compressed when lying in the mirror plane, and elongated outside the plane; conversely in NV_{d2}^0 the bond is stretched when lying in the mirror plane and squeezed out of the plane. We found that the spin density is largely localized at the three $C_{(c)}$ carbon atoms facing the vacancy (μ is +0.883 $|e|$ at each carbon) in NV_q^0. It is +0.800 $|e|$ on the two out of plane carbons and −0.679 $|e|$ on the third carbon in NV_{d1}^0. Finally, it is almost completely localized on the carbon on the mirror plane (+0.851 $|e|$) in NV_{d2}^0.

From our calculations NV_{d1}^0 is the ground state of the NV^0 system; with respect to it, NV_{d2}^0 and NV_q^0 correspond to the lowest spin forbidden and spin conserved excited electronic states, respectively. NV_{d1}^0 is more stable than NV_q^0 by ∼ 0.5 eV, and than NV_{d2}^0 by ∼ 0.2 eV. The process leading to the aggregation between a substitutional nitrogen adjacent to a carbon vacancy (and then to the NV^0 defects) was found energetically favoured, irrespective of the adopted functional and basis set.

The EPR hyperfine coupling tensor has been computed for NV_q^0. The results are in excellent agreement with both experimental and the computed data available in literature. The Raman spectra of the NV^0 defects shows a single peak, at 1315 cm^{-1}, redshifted with respect to the single peak of pristine diamond by only 2 cm^{-1}. The NV^- peak is redshifted by 7 cm^{-1} with respect to the neutral form. Unlike the Raman spectra, unable to distinguish different spin states and only sensible to charge, the IR responses of the three systems (NV_q^0, NV_{d1}^0 and NV_{d2}^0) and the one of NV^- show specific peaks and peak shape; hence IR is able to differentiate spin and charge states.

The present paper shows that the simulated IR and Raman spectra, and the computed hyperfine constants represent powerful tools for discriminating similar defects encountered in natural and synthetic diamonds.

Author contribution

A.M. Ferrari: Conceptualization, formal analysis, writing, project administration, supervision
M. D'Amore: methodology, validation, investigation, writing
K. E. E.-Kelany: simulation, validation, data curation
F. Gentile: simulation, validation, investigation,
R. Dovesi: revision

Declaration of competing interest

The authors declare that they have no known competing financial interests or personal relationships that could have appeared to influence the work reported in this paper.

Acknowledgements

Access to the HPC resources of CINECA (Iscra project HP10CFUGEW) has been appreciated.

Appendix A. Supplementary data

Supplementary data to this article can be found online at https://doi.org/10.1016/j.jpcs.2021.110304.

References

[1] J. Charette, Absorption spectra of type I and type II synthetic diamonds, J. Chem. Phys. 37 (1962) 3014–3015.
[2] H. Dyer, F. Raal, L. Preez, J. Loubser, Optical absorption features associated with paramagnetic nitrogen in diamond, Phil. Mag. 11 (1965) 763–774.
[3] T. Evans, Z. Qi, J. Maguire, The stages of nitrogen aggregation in diamond, J. Phys. C Solid State Phys. 14 (1981) L379.
[4] T.D.A. Zedgenizova, A.A. Kalinin, V.V. Kalinina, Y.N. Palyanov, V.S. Shatsky, The transformation features of impurity defects in natural diamonds of various habits under high P–T conditions, Dokl. Earth Sci. 466 (2016) 32–37.
[5] S.C. Lawson, D. Fisher, D.C. Hunt, M.E. Newton, On the existence of positively charged single-substitutional nitrogen in diamond, J. Phys. Condens. Matter 10 (27) (1998) 6171.
[6] J. Bade, S. Sahaida, B. Stoner, J. Windheim, J. Glass, K. Miyata, K. Nishimura, K. Kobashi, Fabrication of diamond thin-film thermistors for high temperature applications, diamond relat. Mater 2 (1993) 816–819.
[7] P. Bergonzo, D. Tromson, C. Mer, CVD diamond-based semi-transparent beam-position monitors for synchrotron beamlines: preliminary studies and device developments at CEA/saclay, J. Synchrotron Radiat. 13 (2006) 151–158.
[8] G.B.B.M. Sutherland, D.E. Blackwell, W.G. Simeral, The problem of the two types of diamond, Nature 174 (1954) 901–904.
[9] G. Davies, The A nitrogen aggregate in diamond – its symmetry and possible structure, J. Phys. Chem. 9 (1976) L537–L542.
[10] S.J. Breuer, P. Briddon, *Ab initio* investigation of the native defects in diamond and self-diffusion, Phys. Rev. B 51 (11) (1995) 6984–6994.
[11] A. Mainwood, Modelling of interstitial-related defects in diamond, Diam. Relat. Mater. 8 (8) (1999) 1560–1564.
[12] R. Kalish, A. Reznik, S. Prawer, D. Saada, J. Adler, Ion-implantation-induced defects in diamond and their annealing: experiment and simulation, Phys. Status Solidi 174 (1) (1999) 83–99.
[13] G. Davies, B. Campbell, A. Mainwood, M. Newton, M. Watkins, H. Kanda, T. Anthony, Interstitials, vacancies and impurities in diamond, Phys. Status Solidi 186 (2) (2001) 187–198.
[14] J.P. Goss, B.J. Coomer, R. Jones, C.J. Fall, P.R. Briddon, S. Öberg, Extended defects in diamond: the interstitial platelet, Phys. Rev. B 67 (2003) 165208.
[15] J.P. Goss, R. Jones, T.D. Shaw, M.J. Rayson, P.R. Briddon, First principles study of the self-interstitial defect in diamond, Phys. Status Solidi 186 (2) (2001) 215–220.
[16] G. Davies, H. Smith, H. Kanda, Self-interstitial in diamond, Phys. Rev. B 62 (2000) 1528–1531.
[17] R. Kalish, A. Reznik, K.W. Nugent, S. Prawer, The nature of damage in ion-implanted and annealed diamond, Nucl. Instrum. Methods Phys. Res. B 148 (1) (1999) 626–633.
[18] D.J. Twitchen, D.C. Hunt, M.E. Newton, J.M. Baker, T.R. Anthony, W.F. Banholzer, Electron paramagnetic resonance (EPR) and optical absorption studies of defects created in diamond by electron irradiation damage at 100 and 350K, Phys. B Condens. Matter 273 (1999) 628–631.
[19] P.F. Lai, S. Prawer, C. Noble, Electron spin resonance investigation of ion-irradiated diamond, Diam. Relat. Mater. 11 (7) (2002) 1391–1396.
[20] A. Moroño, S.M.G. de Vicente, E.R. Hodgson, Radiation effects on the optical and electrical properties of CVD diamond, Fusion Eng. Des. 82 (15) (2007) 2563–2566.
[21] H. Amekura, N. Kishimoto, Effects of high-fluence ion implantation on colorless diamond self-standing films, J. Appl. Phys. 104 (6) (2008) 63509.
[22] S. Prawer, I. Rosenblum, J.O. Orwa, J. Adler, Identification of the point defects in diamond as measured by Raman spectroscopy: comparison between experiment and computation, Chem. Phys. Lett. 390 (2004) 458–461.
[23] D. Hyde-Volpe, B. Slepetz, M. Kertesz, The [V−C=C−V] divacancy and the interstitial defect in diamond: vibrational properties, J. Phys. Chem. 114 (21) (2010) 9563–9567.
[24] D.N. Jamieson, S. Prawer, K.W. Nugent, S.P. Dooley, Cross-sectional Raman microscopy of MeV implanted diamond, Phys. Rev. B 106 (1995) 641–645.
[25] J.D. Hunn, S.P. Withrow, C.W. White, D.M. Hembree Jr., Raman scattering from MeV-implanted diamond, Phys. Rev. B 52 (1995) 8106–8111.
[26] S. Prawer, K.W. Nugent, D.N. Jamieson, The Raman spectrum of amorphous diamond, Diam. Relat. Mater. 7 (1998) 106–110.
[27] J.O. Orwa, K.W. Nugent, D.N. Jamieson, S. Prawer, Raman investigation of damage caused by deep ion implantation in diamond, Phys. Rev. B 62 (9) (2000) 5461–5472.
[28] R. Brunetto, G.A. Baratta, G. Strazzulla, Raman spectroscopy of ion irradiated diamond, J. Appl. Phys. 96 (2004) 380–386.
[29] P. Olivero, S. Rubanov, P. Reichart, B.C. Gibson, S.T. Huntington, J.R. Rabeau, A. D. Greentree, J. Salzman, D. Moore, D.N. Jamieson, S. Prawer, Characterization of three-dimensional microstructures in single-crystal diamond, Diam. Relat. Mater. 15 (2006) 1614–1621.
[30] A.A. Bergman, A.M. Zaitsev, M. Huang, A. Gorokhovsky, Photoluminescence and Raman studies of Xe ion-implanted diamonds: dependence on implantation dose, J. Lumin. 129 (2009) 1524–1526.
[31] M.W. Doherty, N.B. Mansonb, P. Delaney, F. Jelezko, J. Wrachtrupe, L. C. Hollenberg, The nitrogen-vacancy colour centre in diamond, Phys. Rep. 528 (2013) 1–45.
[32] J.H.N. Loubser, J.A.V. Wyk, Electron spin resonance in the study of diamond, Rep. Prog. Phys. 41 (8) (1978) 1201.
[33] J.H.N. Loubser, J.A.V. Wyk, Electron spin resonance in annealed type 1*b* diamond, Diam. Res. 11 (1977) 4–7.
[34] S. Felton, A.M. Edmonds, M.E. Newton, P.M. Martineau, D. Fisher, D.J. Twitchen, Electron paramagnetic resonance studies of the neutral nitrogen vacancy in diamond, Phys. Rev. B 77 (8) (2008), 081201.
[35] G. Davies, Dynamic Jahn-Teller distortions at trigonal optical centres in diamond, J. Phys. C Solid State Phys. 12 (1979) 2551.
[36] J. Weber, W. Koehl, J. Varley, A. Janotti, B. Buckley, C. Van de Walle, D. Awschalom, Proc. Natl. Acad. Sci. Unit. States Am. 107 (2010) 8513.
[37] F. Jelezko, J. Wrachtrup, J. Phys. Condens. Matter 107 (2004) 1089.
[38] F. Jelezko, J. Wrachtrup, Phys. Status Solidi 203 (2006) 3207.
[39] F. Jelezko, J. Wrachtrup, J. Phys. Condens. Matter 18 (2006) 807.
[40] I. Aharonovich, S. Castelletto, D. Simpson, C.-H. Su, A. Greentree, S. Prawer, Rep. Prog. Phys. 74 (2011), 076501.
[41] P. Hohenberg, W. Kohn, Inhomogeneous electron gas, Phys. Rev. 136 (3B) (1964) B864.
[42] W. Kohn, L.J. Sham, Self-consistent equations including exchange and correlation effects, Phys. Rev. 140 (4A) (1965) A1133.
[43] A.D. Becke, Density-functional thermochemistry. III. The role of exact exchange, J. Chem. Phys. 98 (7) (1993) 5648–5652.
[44] C. Lee, W. Yang, R. Parr, Development of the colle-salvetti correlation-energy formula into a functional of the electron density, Phys. Rev. B 37 (2) (1988) 785–789.
[45] R. Dovesi, A. Erba, R. Orlando, C.M. Zicovich-Wilson, B. Civalleri, L. Maschio, M. Rérat, S. Casassa, J. Baima, S. Salustro, B. Kirtman, Quantum-Mechanical Condensed Matter Simulations with CRYSTAL, Wires 8 (2018), 1360-1–1360-36.
[46] R. Dovesi, F. Pascale, B. Civalleri, K. Doll, N.M. Harrison, I. Bush, P. D'Arco, Y. Noël, M. Rérat, P. Carbonnière, M. Causà, S. Salustro, V. Lacivita, B. Kirtman, A. M. Ferrari, F.S. Gentile, J. Baima, M. Ferrero, R. Demichelis, M. De La Pierre, The crystal code, 1976–2020 and beyond, a long story, J. Chem. Phys. 152 (2020) 204111–1–204111–34, https://doi.org/10.1063/5.0004892.
[47] P. Dirac, A theory of electrons and protons, Proc. R. Soc. A 126 (801) (1930) 360–365.
[48] S.H. Vosko, L. Wilk, M. Nusair, Accurate spin-dependent electron liquid correlation energies for local spin density calculations: a critical analysis, Can. J. Phys. 58 (8) (1980) 1200–1211.
[49] J.P. Perdew, K. Burke, M. Ernzerhof, Generalized gradient approximation made simple, Phys. Rev. Lett. 77 (18) (1996) 3865–3868.
[50] C. Adamo, V. Barone, Toward chemical accuracy in the computation of NMR shieldings: the PBE0 model, Chem. Phys. Lett. 298 (1) (1998) 113–119.
[51] A.V. Krukau, O.A. Vydrov, A.F. Izmaylov, G.E. Scuseria, Influence of the exchange screening parameter on the performance of screened hybrid functionals, J. Chem. Phys. 125 (22) (2006), 224106–224106.
[52] J.S. Binkley, J.A. Pople, W.J. Hehre, Self-consistent molecular orbital methods. 21. Small split-valence basis sets for first-row elements, J. Am. Chem. Soc. 102 (3) (1980) 939–947.
[53] S. Salustro, F. Colasuonno, A.M. Ferrari, M. D'Amore, R.D. William, C. Mackrodt, Substitutional boron and nitrogen pairs in diamond. A quantum mechanical vibrational analysis, Carbon 146 (2019) 709–716.
[54] A. Platonenko, F.S. Gentile, F. Pascal, A.M. Ferrari, M. D'Amore, W.C. Mackrodt, R. Dovesi, Nitrogen substitutional defects in silicon. A quantum mechanical investigation of the structural, electronic and vibrational properties, Phys. Chem. Chem. Phys. 21 (2019) 20939–20950.
[55] A.M. Ferrari, S. Salustro, F. Gentile, W. Mackrodt, R. Dovesi, Substitutional nitrogen atom in diamond. A quantum mechanical investigation of the electronic and spectroscopic properties, Carbon 134 (2018) 354–365.
[56] H. Kjær, S.P.A. Sauer, Pople style basis sets for the calculation of NMR spin-spin coupling constants: the 6- 31G-J and 6-311G-J basis sets, J. Chem. Theor. Comput. 7 (2011) 4070–4076.
[57] A.M. Zaitsev, Optical Properties of Diamond - A Data Handbook, Springer-Verlag, 2001.
[58] J. Walker, Optical absortpion and luminescence in diamond, Rep. Prog. Phys. 42 (1979) 1605–1659.
[59] M. Cardona, M.L.W. Tewalt, Isotope effects on the optical spectra of semiconductors, Rev. Mod. Phys. 77 (4) (2005) 1173.
[60] A. Ferrari, K. El-Kelany, F.S. Gentile, M. D'Amore, R. Dovesi, The NV−….N+ Charged Pair in Diamond: a Quantum-Mechanical investigation, Phys. Chem. Chem. Phys. (2021). Accepted Manuscript, https://doi.org/10.1039/D1CP02436A.
[61] A.M. Ferrari, K. El-Kelany, F.S. Gentile, M. D'Amore, R. Dovesi, The Quantum Mechanical Investigation of the Epr Response of the NV Negatively Charged Defect in Diamond, 2021 (submitted) for publication, https://doi.org/10.1039/D1CP02363B.
[62] M.S. Barson, E. Krausz, N.B. Manson, M.W. Doherty, The fine structure of the neutral nitrogen-vacancy center in diamond, Nanophotonics 8 (11) (2019) 1985–1991, https://doi.org/10.1515/nanoph-2019-0142.
[63] A. Gali, Theory of the neutral nitrogen-vacancy center in diamond and its application to the realization of a qubit, Phys. Rev. B 79 (2009) 235210.
[64] H. Bower, M. Symons, Electron spin resonance spectra associated with nitrogen in diamonds, Nature 210 (1966) 1037–1038.
[65] F.L. Hirshfeld, Bonded atom fragments for describing molecular charge distributions, Theor. Chem. Acc. 44 (1977) 129–138.

[66] R. Bader, Atoms in Molecules, Clarendon.
[67] R.O. Lowdin, On the non-orthogonality problem connected with the use of atomic wave functions in the theory of molecules and crystals, J. Chem. Phys. 18 (1950) 365–375.
[68] M. Causà, M. D'Amore, C. Garzillo, F. Gentile, A. Savin, The bond analysis techniques (elf and maximum probability domains) application to a family of models relevant to bio-inorganic chemistry, Struct. Bond 150 (2013) 119–142, https://doi.org/10.1007/978-3-642-32750-6_4.
[69] M. Causà, M. D'Amore, F. Gentile, M. Menendez, M. Calatayud, Electron localization function and maximum probability domains analysis of semi-ionic oxides crystals, surfaces and surface defects, Computational and Theoretical Chemistry 1053 (2015) 315–321, https://doi.org/10.1016/j.comptc.2014.11.001.